NANO LETTERS

Letter

pubs.acs.org/NanoLett

Plasmonically Enhanced Thermomechanical Detection of Infrared Radiation

Fei Yi, Hai Zhu, Jason C. Reed, and Ertugrul Cubukcu*

Department of Materials Science and Engineering, University of Pennsylvania, Philadelphia, Pennsylvania, 19104, United States

Supporting Information

ABSTRACT: Nanoplasmonics has been an attractive area of research due to its ability to localize and manipulate freely propagating radiation on the nanometer scale for strong light-matter interactions. Meanwhile, nanomechanics has set records in the sensing of mass, force, and displacement. In this work, we report efficient coupling between infrared radiation and nanomechanical resonators through nanoantenna enhanced thermoplasmonic effects. Using efficient conversion of electromagnetic energy to mechanical energy in this plasmo-thermomechanical platform with a nanoslot plasmonic absorber integrated directly on a nanobeam mechanical resonator, we demonstrate room-temperature detection of nanowatt level power fluctuations in infrared radiation. We expect our approach, which combines nanoplasmonics with nanomechanical resonators, to lead to optically controlled nanomechanical systems enabling unprecedented functionality in biomolecular and toxic gas sensing and on-chip mass spectroscopy.

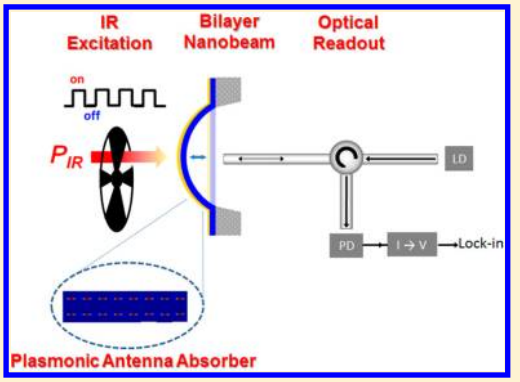

KEYWORDS: *Plasmonic antennas, thermoplasmonics, thermomechanics, infrared sensor, bimetallic nanobeam, fiber-optic Fabry−Perot interferometer*

The nanoscale light concentration and near-field enhancement available to resonant metallic nanostructures have been a driving force in nanoplasmonics.[1−3] Along these lines, plasmonic nanoantennas have been utilized in a broad range of applications involving strong light-matter interactions.[4−13] Recently, thermoplasmonics, which take advantage of photothermal effects induced by resonant light absorption in metallic nanostructures,[14−18] has emerged as a new research direction enabling nanoscale heat sources. These effects have been investigated for different applications, such as photothermal cancer therapy[19−21] and thermophotovoltaics.[22,23] On a different front, nanomechanics is a vibrant research field in nanoscience that has generated both academic and industrial interest for its promise in novel sensor applications.[24−30] Inspired by the Golay cell, an optomechanical thermal detector,[31] thermally actuated bilayer cantilever based micromechanical structures have been invented and used as optomechanical focal plane arrays for detection of infrared (IR)[32−36] and terahertz[37] radiation.

In this Letter, we propose a new plasmo-thermomechanical device platform, which integrates thermoplasmonic effects with nanomechanics using light absorption by plasmonic nanoantennas as the nanoscale heat source inducing thermomechanical actuation. As one specific example of the platform, we report a novel room-temperature thermal infrared detector that integrates a nanoplasmonic absorber on a beam type nanomechanical structure. Our nanoplasmonic thermomechanical device relies on efficient absorption of infrared radiation by an array of nanoslot antennas as an active component that converts optical power into heat. The nanoslot configuration provides the best thermomechanical coupling due to its uniform bilayer material coverage as compared to an array of discrete nanoantenna elements. The generated heat is then converted to a temperature increase on the integrated nanomechanical bimaterial structure. In response to this temperature increase, the bimaterial nanomechanical beam bends as a result of the differences in the thermal expansion coefficients of the two constituent materials. An integrated fiber-based interferometric readout, which offers the best displacement sensitivity, then converts this mechanical bending into an electrical signal.[38]

As shown in Figure 1, the active structure of the plasmo-thermomechanical IR detector (PlasMIRD) is a suspended 100 μm by 500 μm gold−silicon nitride bilayer beam integrated with the plasmonic nanoantenna absorber. The bilayer beam consists of a 22 nm thick gold layer with 3 nm of titanium for adhesion on 100 nm of silicon nitride. The plasmonic absorber, embedded in the metal layer, consists of an array of nanoslot antennas etched into the bilayer mechanical beam, which is designed to enhance the absorption of the IR radiation with a spectrum centered around a wavelength λ = 6 μm.[39] Typical nanoslots are 100 nm wide and 1600 nm long (see Figure S1 in Supporting Information). We refer to the absorption efficiency of the bilayer structure with integrated nanoantenna absorber as

Received: January 8, 2013
Revised: March 7, 2013

   dx.doi.org/10.1021/nl400087b | *Nano Lett.* XXXX, XXX, XXX−XXX

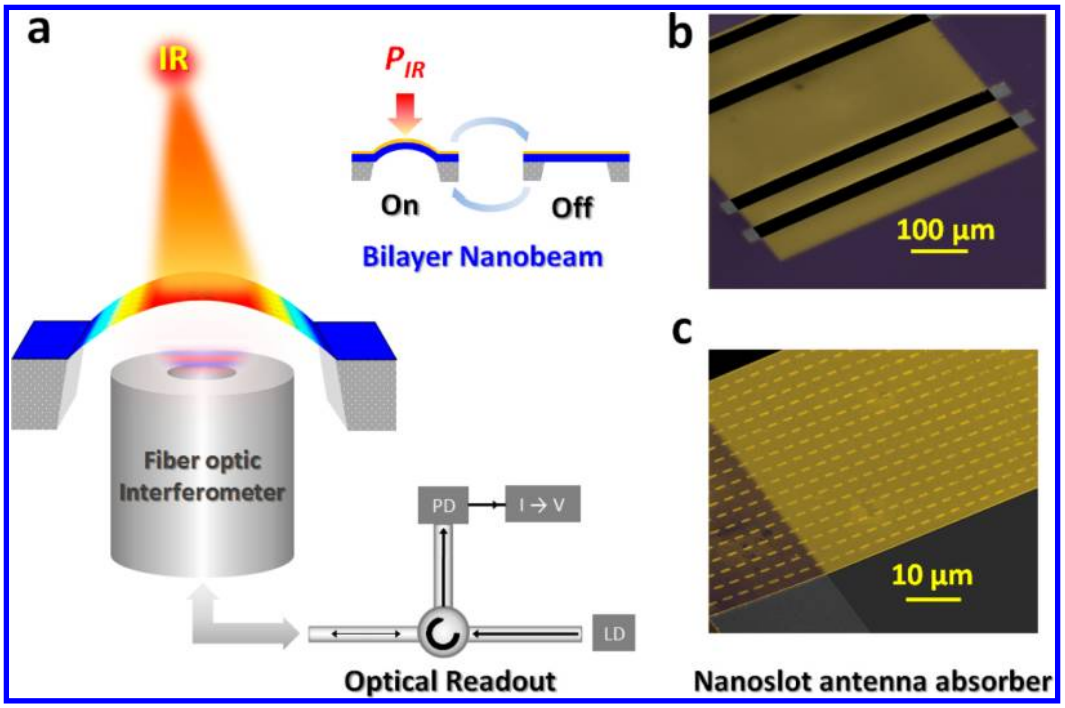

Figure 1. An overview of the plasmo-thermomechanical IR detector (PlasMIRD). (a) A nanoslot antenna array is embedded in the gold layer of a bimetallic beam structure. The IR radiation is converted into heat by the nanoantenna array and causes temperature increase in the bilayer structure. The increased temperature causes the bilayer structure to deflect due to the mismatch between the thermal expansion coefficients of the gold and silicon nitride layers. The bilayer beam is one of the two reflectors of a fiber optic Fabry–Perot interferometer (FFPI). The deflection of the bilayer beam is read out optically by the FFPI. False color SEM images of the (b) bilayer beam and (c) the integrated nanoslot absorber.

η_{ant} and the absorbed IR power as $P_{abs} \equiv P_{IR} \times \eta_{ant}$, where P_{IR} is the total incident IR power. In previous studies, it has been reported that a single layer of an array of plasmonic nanoantennas can be used as an efficient infrared absorber without a back reflector metal plate used in perfect metamaterial based absorbers.[40−42] The plasmonic nanoslot antenna absorber used in this study converts the freely propagating IR radiation into a localized current that is dissipated into heat due to the finite conductance of gold at these frequencies, similar to Ohmic dissipation in a resistive electrical circuit. The mechanical deflection of the bilayer nanobeam driven by the thermal energy is then read out optically, as diagramed in Figure 1a.

In order to optimize the photothermal conversion efficiency of the plasmonic antenna absorber, we first used a finite element method based simulation software package to numerically study the optical properties of nanoslot antenna absorber employing periodic boundary conditions and plane wave excitation.[43] Figure 2a shows the simulated unit cell that consists of a nanoslot antenna in a 25 nm thick metal layer (3 nm of Ti and 22 nm of Au) on top of a 100 nm thick silicon nitride substrate. The nanoslot antennas were excited by a plane electromagnetic wave polarized along the short axis of the antenna, as opposed to the case of a nanorod antenna that requires the electric field to be polarized along its length for resonance excitation. The power transmission (T) and reflection (R) coefficients are first calculated to determine the absorption efficiency defined as $\eta_{ant} = 1 - T - R$, which was confirmed to be valid through near-field power dissipation calculations for the structure.[39] Figure 2b shows the induced near field distribution in the slot region, clearly showing that the electromagnetic energy is strongly localized in the slot region. We followed the same procedure as in our previous study[39] to optimize the dimensions of the nanoslot antennas (see Figure S1 in the Supporting Information).

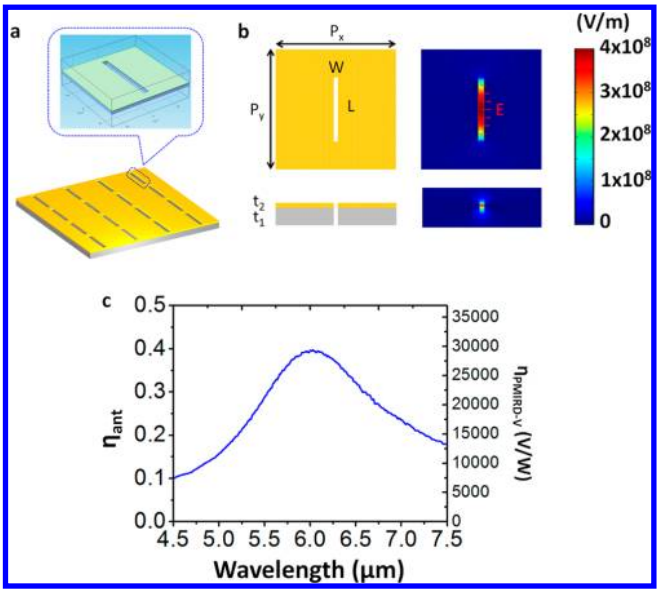

Figure 2. The simulation and measurement of the resonant nanoslot plasmonic antennas. (a) A unit cell of the studied nanoslot antennas etched into the gold layer with periodic boundary conditions. The thicknesses of the silicon nitride and metal layers are t_1 = 100 nm and t_2 = 25 nm, respectively (Ti/Au = 3 nm/22 nm). (b) The schematic diagram of the unit cell and the near field distribution in the slot. (c) The typical measured absorption spectrum and the corresponding detector responsivity of the nanoslot antennas with $p_x = p_y = 3$ μm, W = 100 nm, and L = 1.6 μm.

dx.doi.org/10.1021/nl400087b | Nano Lett. XXXX, XXX, XXX−XXX

The nanoslot antennas were optimized by these numerical calculations and fabricated by etching all the way through into the free-standing bilayer mechanical beam. A thickness ratio between the gold and nitride of 1:4 was previously reported to be the optimized value for maximum mechanical deflection (see Figure S2e in the Supporting Information).[33,34] Figure 2c shows the typical measured absorption spectrum of the nanoslot antenna array. The measured peak absorption of 40% occurs at a resonant wavelength of 6 μm in agreement with absorption for a single layer of resonant nanostructured metal sheet on a substrate without a metal back reflector.[44] Since the metal thickness is constrained by the thickness ratio of gold and silicon nitride for maximum mechanical deflection, the nanoslot design offers about 10 times larger absorption compared to that of a uniform metal layer of the same thickness.[39] The gold nanoantennas resonantly capture the incident energy and effectively dissipate it into heat.[45] Unity optical absorption can be achieved using a metal back reflector on the other side of the silicon nitride layer to enhance the plasmonic resonance. However, adding the back reflector on the other side of the bilayer structure would reduce its mechanical deflection.

The second stage of the plasmo-thermomechanical IR detection is the thermomechanical actuation of the bilayer nanobeam. The absorbed IR power causes an increased temperature ΔT in the bilayer nanobeam. The rate of temperature increase in a bilayer nanobeam of length l and width w per unit absorbed IR power, defined as $\eta_{T/P} \equiv \Delta T/P_{abs}$, is found by solving the (one-dimensional) 1D heat transfer equation[46,47]

$$\frac{d^2}{dx^2}T(x,t) + \frac{1}{\kappa}g(x,t) = \frac{1}{\alpha}\frac{d}{dt}T(x,t) \quad (1)$$

In our thermal analysis, we assumed that the midpoint located at $x = 0$ is initially held at a constant temperature $T(x, t = 0) = T_0 = 300$ K, same as the two ends of the beam modeled to be perfect heat sinks. Here, $\kappa = (\kappa_1 t_1 + \kappa_2 t_2)/(t_1+t_2)$ is the thermal conductivity and $\alpha = (\kappa_1 t_1 + \kappa_2 t_2)/(\rho_1 C_1 t_1 + \rho_2 C_2 t_2)$ is the thermal diffusivity of the composite beam averaged over the thickness, where ρ, C, and t are, respectively, the mass density, the specific heat, and the layer thickness. The subscripts 1 and 2 refer to the gold and nitride layers, respectively. The heat generation density $g(x,t)$ is proportional to the absorbed infrared power P_{abs} and can have different spatial profiles depending on the illumination source; that is, point source at the center of the beam, uniform source along the beam, or Gaussian beam source. The steady state solution of eq 1 for the uniform heating case(shown in Figure 3a) is given by

$$T(x) = \frac{\left[\left(\frac{l}{2}\right)^2 - \left(\frac{x}{2}\right)^2\right]P_{abs}}{2(\kappa_1 n + \kappa_2)t_2 w l} + T_0(-l/2 < x < l/2) \quad (2)$$

The Green's function method solutions for point source and Gaussian beam source heating are given in the Supporting Information. We also used a finite element method code to solve the heat transfer problem in the bilayer structure and found perfect agreement with the analytical solution. Figure 3b shows the exponential increase of the temperature difference $\Delta T_0(t)$ at the center of the beam. The $1/e$ time constant τ was found to be about 0.55 ms for all the three heating profiles. From the linear relationship between ΔT_0 and P_{abs}, as shown in Figure 3d,we found $\eta_{T/P}$ to be 1.18×10^5 K/W for point source heating, 9.13×10^4 K/W for Gaussian source heating, and 5.9×10^4 K/W for uniform heating (see Figure S2 in the Supporting Information). The induced temperature difference ΔT in turn causes the bilayer structure to expand and deflect due to the mismatch between the thermal expansion coefficients γ of silicon nitride and gold. The temperature induced bending of the bilayer beam can be calculated analytically using the following differential equation[48]

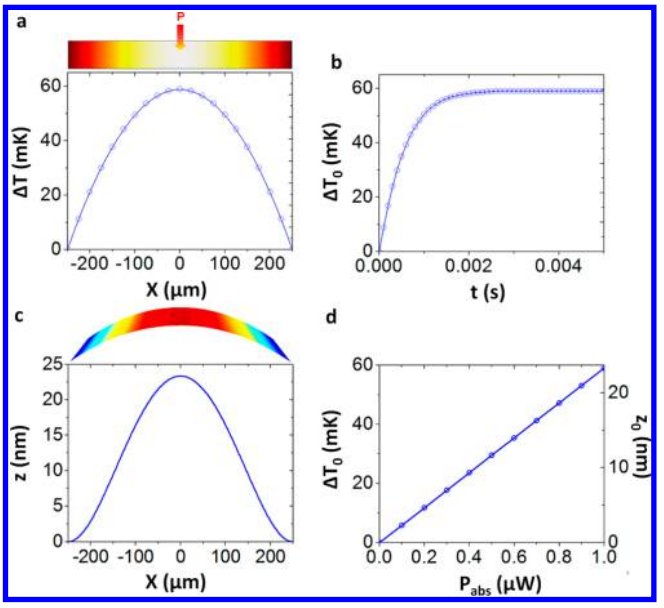

Figure 3. The simulation results for the heat transfer and mechanical deflection problems. (a) The steady-state temperature difference distribution ΔT along a bilayer beam under uniform infrared illumination and the corresponding linescan at the midpoint. The total absorbed power $P_{abs} = 1$ μW. (b) The temporal evolution of ΔT_0, temperature difference at the center of the beam. (c) The 2D distribution of steady state deflection z in a bilayer beam caused by the temperature increase. The two sides of the bilayer beam are set to be mechanically fixed. (d) The steady-state temperature increase ΔT_0 and the mechanical deflection z_0 as a function of the absorbed power P_{abs}. The material properties used in the simulation are listed Table S1 in the Supporting Information.

$$\frac{d^2z}{dx^2} = 6(\gamma_2 - \gamma_1)\frac{t_1 + t_2}{t_2^2 K}\Delta T(x) \quad (3)$$

Here, the dimensionless parameter $K = 4 + 6n + 4n^2 + (E_1/E_2)n^3 + (E_2/E_1)n^{-1}$ is defined in terms of the Young's moduli of the two materials ($E_{1,2}$), the layer thicknesses ($t_{1,2}$), and the thickness ratio $n = t_1/t_2$. The detailed analytical solutions of eq 3 are provided in the Supporting Information. Figure 3c shows the rigorous 3D numerical simulation results of the mechanical deflection along the bilayer structure for uniform source. The thermomechanical conversion factor $\eta_{z/P} \equiv z/P_{abs}$ is found to be 0.047, 0.036, and 0.023 m/W for the point source, Gaussian beam, and uniform heating, respectively (see Figure S2d in the Supporting Information).

In order to measure the bilayer nanobeam deflection, z, we use a fiber optic interferometer that offers the best displacement sensitivity[38] based on a Fabry–Perot cavity formed between the facet of a cleaved fiber and the nanobeam. Output of a very low noise external cavity diode laser of 1550 nm wavelength is coupled into the cleaved probe fiber through a fiber-optic circulator whose return port is connected to a shot-noise limited small area PIN photodiode. The light reflected by the

dx.doi.org/10.1021/nl400087b | Nano Lett. XXXX, XXX, XXX–XXX

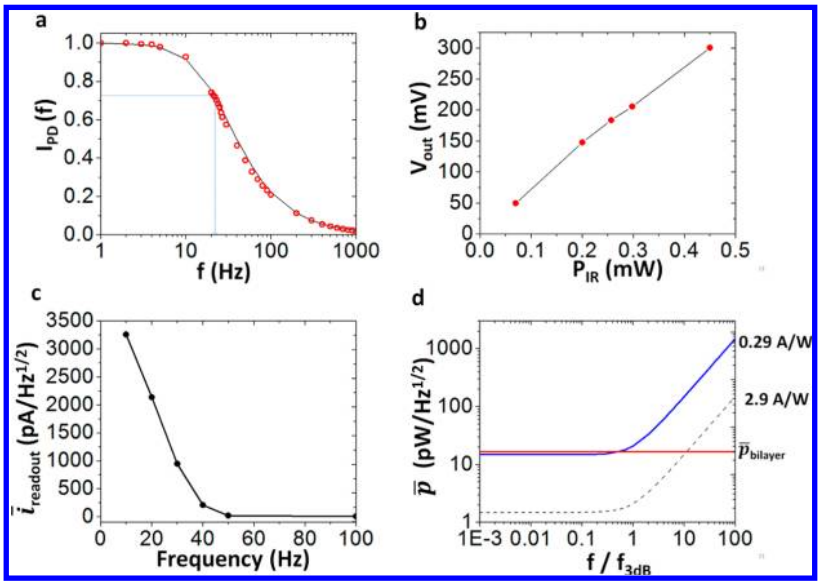

Figure 4. The measured responsivity and noise equivalent power of the PlasMIRD. (a) The normalized frequency response of the PlasMIRD measured using a modulated 405 nm laser as the excitation. (b) The relationship between the response of the PlasMIRD at 1000 Hz and the input IR power. The vertical axis is the output voltage of the current to voltage converter, measured by the lock-in amplifier. The horizontal axis is the IR power received by the nanobeam. (c) $1/f$ spectral density noise of the readout system. (d) The total bilayer noise density $\bar{p}_{bilayer}$, including thermal fluctuation noise, background fluctuation noise, and thermomechanical vibration noise (the red solid line), and the optical readout noise equivalent power $\bar{p}_{readout}$. (the blue solid line for $\eta_{PlasMIRD}$ = 0.29 A/W and the black dash line for $\eta_{PlasMIRD}$= 2.9 A/W).

cleaved end facet of the fiber and the nanobeam will interfere with each other. Therefore, the total reflected optical power, P_{FPr}, is very sensitive to the change z in the distance between the bilayer mechanical beam and the facet of the fiber, that is, the cavity length, allowing us to measure the nanobeam deflection z. The power sensitivity of the interferometer, η_{FP}, is the change in reflected power per unit deflection, that is, $\eta_{FP} = dP_{FPr}/dz$, which reaches its maximum value for cavity lengths equal to an integer multiple of a quarter wavelength (see Figure S3c in the Supporting Information). The changes in the mechanical bending of the bilayer structure yields changes in the photocurrent given by $\Delta I_{PD} \equiv \eta_{PD} \times \eta_{FP} \times z$, where η_{PD} is the quantum efficiency of the photodiode. For an interferometer input of 1 mW, η_{PD} = 0.886 A/W, and R = 0.037 (the power reflection coefficient for the end facet of a bare fiber). The maximum power sensitivity at the quadrature point of interferometer is therefore η_{FP} = 0.318 μW/nm and the current sensitivity $\eta_{FP\text{-}I} = \eta_{PD} \times \eta_{FP}$ = 0.282 μA/nm, which agrees well with the measurements (see Figure S3b in the Supporting Information). In the last stage of the plasmo-thermomechanical detector, the signal current I_{PD} is converted by a current to voltage converter with a resistance R_{IV} into an output voltage $V_{OUT} = I_{PD} \times R_{IV}$. The signal voltage V_{OUT} is therefore related to the input IR power P_{IR} by

$$V_{OUT} = P_{IR} \times \eta_{ant} \times \eta_{T/P} \times \eta_{z/T} \times \eta_{FP} \times \eta_{PD} \times R_{IV} \equiv P_{IR} \times \eta_{PlasMIRD} \quad (4)$$

, where $\eta_{PlasMIRD}$ is defined as the voltage responsivity of the PlasMIRD.

One of the important characteristics for a detector is its responsivity, the measure of how efficiently the detector can convert optical power to electrical power. We experimentally characterized the responsivity of the fabricated devices using two different lasers. A 405 nm diode laser that can be sinusoidally modulated is used as the heat source for the measurement of the temporal characteristics of the photothermal response. The typical normalized frequency response of the PlasMIRD is shown in Figure 4a. The 3 dB cutoff frequency, f_{3dB}, is found to be 23 Hz corresponding to a time constant $\tau = 1/(2\pi f_{3\,dB})$ = 6.9 ms.

For the infrared photoresponse of PlasMIRD, we use the output of a continuous wave quantum cascade laser (QCL) of ~6 μm wavelength modulated by a mechanical chopper (see Figure S4 in the Supporting Information). The chopper frequency is set at 1000 Hz. In order to study the dependence of the PlasMIRD response on the input IR power, we reduced the P_{IR} from 0.45 mW and monitored I_{PD}. Figure 4b shows that there is a linear relationship between the normalized response of PlasMIRD and the input IR power in agreement with the theoretical prediction. By using the measured frequency dependence of the photothermal response in Figure 4a, we can estimate the voltage responsivity as 29 kV/W for $R_{IV} = 10^5$ V/A in the low frequency limit.

Since in many applications the primary objective is measuring small signals, the most important performance parameter for a detector is, arguably, its noise equivalent power (NEP), which is a direct measure of the smallest optical power that can be measured. The NEP of a detector is limited by the fluctuations in the output voltage, without any input infrared power, originating from nonequilibrium thermodynamical processes and quantum statistics of photons and electrons in the detection system. In our detector there are two main parts of the detection system, namely, the interferometric read out system and the bilayer nanobeam, that contribute to the detector noise. For the bilayer nanobeam, the fundamental sources of noise are (1) the thermal fluctuation noise, similar to Johnson noise in a resistor due to the finite thermal conductance of the bilayer structure, (2) background fluctuation noise due to the radiative heat exchange with the environment, and (3) thermomechanical noise originating from the thermal energy of the mechanical modes.[49] The details of

dx.doi.org/10.1021/nl400087b | Nano Lett. XXXX, XXX, XXX−XXX

the NEP calculations for each contribution are given in the Supporting Information. The thermal fluctuation noise $\overline{p}_{th}$ due to the heat exchange between the bilayer beam and the supporting silicon frame through the two "legs" of the bilayer beam amounts to 6.5 pW/Hz$^{-1/2}$. The background fluctuation noise $\overline{p}_{RAD}$ which accounts for the random fluctuations in temperature due to the heat exchange between the bilayer beam and the environment through radiation is found to be 1.2 pW/Hz$^{-1/2}$. The off-resonance thermomechanical[50,51] vibration noise $\overline{p}_{vib}$ arising from the thermal energy of the bilayer beam can be calculated as 17 fW/Hz$^{1/2}$ using the measured mechanical to optical conversion efficiency along with the mechanical resonance frequency (146.6 kHz) and the quality factor ($Q \sim 980$). We can define the total noise from the bilayer structure as

$$\overline{p}_{bilayer} = \frac{\sqrt{\overline{p}_{th}^2 + \overline{p}_{RAD}^2 + \overline{p}_{vib}^2}}{\eta_{ant}} \quad (5)$$

By plugging in the values calculated above and the measured η_{ant}, $\overline{p}_{bilayer}$ is calculated to be 16.5 pW/Hz$^{1/2}$ in the low frequency limit. It is clear that the main contribution to $\overline{p}_{bilayer}$ is from the thermal fluctuation noise $\overline{p}_{th}$.

The interferometric read-out setup is limited by two fundamental noise sources: (1) the shot noise of the PIN photodetector and (2) the relative intensity noise (RIN) of the 1550 nm laser originating from spontaneous emission. We find the total read-out current noise, dominated by the photodetector shot noise, to be $\overline{i}_{readout}$ = 4.3 pA/Hz$^{1/2}$ (see Supporting Information). In the low frequency limit, this corresponds to an NEP, $\overline{p}_{readout}$ = 14.8 pW/Hz$^{1/2}$. For higher frequencies the thermal responsivity (Figure 4a) needs to be taken into account.

We also need to consider the $1/f$ noise for the low-frequency region. As seen in the measured noise spectrum (Figure 4c), our optical readout system is dominated by the $1/f$ noise when the operation frequency is below 50 Hz. Above 50 Hz, shot noise and RIN noise are the major contributions. Therefore the requirement imposed by $1/f$ noise is that the operation frequency of the PlasMIRD should be above 50 Hz.

Figure 4d shows the frequency dependence of $\overline{p}_{readout}$ and $\overline{p}_{bilayer}$. Since $\overline{p}_{readout}$ also depends on the responsivity of the PlasMIRD due to the frequency dependence of the thermal responsivity. It can be seen that for the measured responsivity of 0.29 A/W, the dominant noise originates from the bilayer nanobeam in the low frequency limit ($f < f_{3\ dB}/2$) and from the read-out setup for $f > f_{3\ dB}/2$. Since the operation frequency needs to be above 50 Hz due to the $1/f$ noise and the measured $f_{3\ dB}$ = 23 Hz, the PlasMIRD is limited by the readout noise when $\eta_{PlasMIRD}$= 0.29 A/W. At 50 Hz we have $\overline{p}_{total} = (\overline{p}_{bilayer}^2 + \overline{p}_{readout}^2)^{1/2}$ = 39 pW/Hz$^{1/2}$ dominated by $\overline{p}_{readout}$ = 35 pW/Hz$^{1/2}$. If the responsivity is increased by 10 times by optimizing the sensitivity of the interferometer, $\overline{p}_{readout}$ is reduced to 1.48 pW/Hz$^{1/2}$ and $\overline{p}_{total}$ is limited by $\overline{p}_{bilayer}$ = 16.5 pW/Hz$^{1/2}$ when $f < 11 \times f_{3\ dB}$ = 253 Hz. Therefore when $\eta_{PlasMIRD}$ = 2.9 A/W, the PlasMIRD is thermal fluctuation noise limited if the operation frequency is between 50 Hz and 253 Hz, and the thermal fluctuation noise equivalent power $\overline{p}_{bilayer}$ = 16.5 pW/Hz$^{1/2}$.

In order to reach the thermal fluctuation noise limit, there are several ways to increase the responsivity. (1) Coating the fiber with metal layer to increase the reflectivity R of the end surface of the fiber. As discussed in the Supporting Information about the fiber-optic Fabry–Perot interferometer (FFPI), if R of the two reflectors in the interferometer is increased from 0.037 to 0.6, the sensitivity of the interferometer η_{FP} will increase by 18 times. (2) Increase the power of the detecting light P_{1550}, because the sensitivity of the interferometer also increases linearly with the power of the detecting light. (3) Optimizing the bilayer structure to achieve larger deflection.

In the current version of the PlasMIRD, we measured the NEP to be 5nW/Hz$^{1/2}$ at 1 kHz, which is already comparable to that of commercially available thermal infrared detectors.[52] We believe that the NEP of this initial device is limited by the microphonic pickup of ambient noise by the cleaved fiber of ~1 cm length used in the interferometer setup. In a commercial implementation of our detector, the silicon bench technology[53] can be used to reduce the length of the fiber extension length to ~100 μm, substantially eliminating the microphonic noise.

There are several approaches that can be taken to optimize the responsivity and the speed of our detector. For example, to improve the responsivity employing a distributed nanorod antenna absorber with back reflector can achieve unity IR absorption without reducing the mechanical deflection. The nanobeam can be modified to nanocantilever to obtain larger deflection. As discussed before, the sensitivity of the fiber optic interferometric readout can also be improved.. The time constant, τ, like other thermal IR detectors, is on the order of miliseconds, but it can be optimized by shortening the length L of the nanobeam or cantilever since $\tau \sim 1/L^2$, although the responsivity will be reduced as a trade-off. Compared to quantum detectors in this range of the electromagnetic spectrum, our thermal detector has the advantage of room temperature (uncooled) operation.

We have demonstrated detection of infrared radiation with a performance comparable to the state-of-the-art thermal detectors by a plasmo-thermomechanical detector that utilizes a plasmonic nanoantenna based infrared absorber as an integrated part of a nanomechanical resonator with a novel interferometric fiberoptic read-out. With further improvement in the device implementation, our simulations predict that the minimum detectable optical power can be decreased by 2 orders of magnitude outperforming commercially available thermal infrared detectors. Although the demonstrated PlasMIRD detects mid-IR radiation at 6 μm, its working wavelength range can be tuned to near-infrared or terahertz region by modifying the dimensions of the nanoantenna absorber.[37,54] Broadband IR detection can be realized by integrating nanoantennas with different resonant wavelengths onto the detector. We believe that our approach that uniquely combines advantages of nanoplasmonics and nanomechanics on a compact device platform will open up innovative research directions in on-chip surface enhanced biomolecular infrared and mass spectroscopies.

■ ASSOCIATED CONTENT

Ⓢ Supporting Information

Theoretical simulation and experimental optimization of plasmonic nanoslot antenna absorber; the analytical solution to the heat transfer equation by green's function method; the analytical solution of the mechanical deflection of the bilayer structure; Fiber-optic Fabry–Perot interferometer; measurement of the photoresponse and the noise performance of the PlasMIRD; detailed analysis of the fundamental noise sources in the PlasMIRD; and characterization of the mechanical resonance frequency and quality factor of the bilayer beam.

dx.doi.org/10.1021/nl400087b | Nano Lett. XXXX, XXX, XXX–XXX

This material is available free of charge via the Internet at http://pubs.acs.org.

AUTHOR INFORMATION

Corresponding Author

*E-mail: cubukcu@seas.upenn.edu.

Notes

The authors declare no competing financial interests.

ACKNOWLEDGMENTS

This work was supported partially by the MRSEC Program of NSF under Award Number DMR11-20901 and Penn URF. Parts of this work were carried out in the University of Pennsylvania Nanofabrication Facility, Nano/Bio Interface Center (NBIC) that receives partial support from NSF and the Penn Regional Nanotechnology Facility (PRNF), which is a member of the NSF-funded Materials Research Facilities Network via the MRSEC program.

REFERENCES

(1) Novotny, L. *The Bridge* **2009**, *39* (4), 14−20.
(2) Bharadwaj, P.; Deutsch, B.; Novotny, L. *Adv. Opt. Photonics* **2009**, *1* (3), 438−483.
(3) Novotny, L.; van Hulst, N. *Nat. Photonics* **2011**, *5* (2), 83−90.
(4) Tang, L.; Kocabas, S. E.; Latif, S.; Okyay, A. K.; Ly-Gagnon, D. S.; Saraswat, K. C.; Miller, D. A. B. *Nat. Photonics* **2008**, *2* (4), 226−229.
(5) Cubukcu, E.; Yu, N. F.; Smythe, E. J.; Diehl, L.; Crozier, K. B.; Capasso, F. *IEEE J. Sel. Top. Quantum Electron.* **2008**, *14* (6), 1448−1461.
(6) Cubukcu, E.; Capasso, F. *Appl. Phys. Lett.* **2009**, *95* (20), 201101−201101−3.
(7) Cao, L. Y.; Park, J. S.; Fan, P. Y.; Clemens, B.; Brongersma, M. L. *Nano Lett.* **2010**, *10* (4), 1229−1233.
(8) Cubukcu, E.; Kort, E. A.; Crozier, K. B.; Capasso, F. *Appl. Phys. Lett.* **2006**, *89*, 093120.
(9) Pillai, S.; Catchpole, K. R.; Trupke, T.; Green, M. A. *J. Appl. Phys.* **2007**, *101*, 093105.
(10) Anker, J. N.; Hall, W. P.; Lyandres, O.; Shah, N. C.; Zhao, J.; Van Duyne, R. P. *Nat. Mater.* **2008**, *7* (6), 442−453.
(11) De Wilde, Y.; Formanek, F.; Carminati, R.; Gralak, B.; Lemoine, P. A.; Joulain, K.; Mulet, J. P.; Chen, Y.; Greffet, J. J. *Nature* **2006**, *444* (7120), 740−743.
(12) Schuller, J. A.; Taubner, T.; Brongersma, M. L. *Nat. Photonics* **2009**, *3* (11), 658−661.
(13) Novotny, L.; Stranick, S. J. *Annu. Rev. Phys. Chem.* **2006**, *57*, 303−331.
(14) Govorov, A. O.; Richardson, H. H. *Nano Today* **2007**, *2* (1), 30−38.
(15) Richardson, H. H.; Hickman, Z. N.; Govorov, A. O.; Thomas, A. C.; Zhang, W.; Kordesch, M. E. *Nano Lett.* **2006**, *6* (4), 783−788.
(16) Wang, J.; Chen, Y. T.; Chen, X.; Hao, J. M.; Yan, M.; Qiu, M. *Opt. Express* **2011**, *19* (15), 14726−14734.
(17) Baffou, G.; Quidant, R.; Girard, C. *Appl. Phys. Lett.* **2009**, *94*, 15.
(18) Baffou, G.; Quidant, R.; de Abajo, F. J. G. *ACS Nano* **2010**, *4* (2), 709−716.
(19) Loo, C.; Lin, A.; Hirsch, L.; Lee, M. H.; Barton, J.; Halas, N. J.; West, J.; Drezek, R. *Technol. Cancer Res. Treat.* **2004**, *3* (1), 33−40.
(20) Lal, S.; Clare, S. E.; Halas, N. J. *Acc. Chem. Res.* **2008**, *41* (12), 1842−1851.
(21) O'Neal, D. P.; Hirsch, L. R.; Halas, N. J.; Payne, J. D.; West, J. L. *Cancer Lett.* **2004**, *209* (2), 171−176.
(22) Han, S.; Norris, D. *Opt. Express* **2010**, *18* (5), 4829−4837.
(23) Wu, C.; Neuner, B., III; John, J.; Milder, A.; Zollars, B.; Savoy, S.; Shvets, G. *J Opt.* **2012**, *14* (2), 024005.
(24) Sun, X. K.; Zheng, J. J.; Poot, M.; Wong, C. W.; Tang, H. X. *Nano Lett.* **2012**, *12* (5), 2299−2305.
(25) Naik, A. K.; Hanay, M. S.; Hiebert, W. K.; Feng, X. L.; Roukes, M. L. *Nat. Nanotechnol.* **2009**, *4* (7), 445−450.
(26) Yang, Y. T.; Callegari, C.; Feng, X. L.; Ekinci, K. L.; Roukes, M. L. *Nano Lett.* **2006**, *6* (4), 583−586.
(27) Jensen, K.; Kim, K.; Zettl, A. *Nat. Nanotechnol.* **2008**, *3* (9), 533−537.
(28) Teufel, J. D.; Donner, T.; Castellanos-Beltran, M. A.; Harlow, J. W.; Lehnert, K. W. *Nat. Nanotechnol* **2009**, *4* (12), 820−823.
(29) LaHaye, M. D.; Buu, O.; Camarota, B.; Schwab, K. C. *Science* **2004**, *304* (5667), 74−77.
(30) Knobel, R. G.; Cleland, A. N. *Nature* **2003**, *424* (6946), 291−293.
(31) Kenny, T. W.; Kaiser, W. J.; Waltman, S. B.; Reynolds, J. K. *Appl. Phys. Lett.* **1991**, *59* (15), 1820−1822.
(32) Barnes, J. R.; Stephenson, R. J.; Welland, M. E.; Gerber, C.; Gimzewski, J. K. *Nature* **1994**, *372* (6501), 79−81.
(33) Barnes, J. R.; Stephenson, R. J.; Woodburn, C. N.; Oshea, S. J.; Welland, M. E.; Rayment, T.; Gimzewski, J. K.; Gerber, C. *Rev. Sci. Instrum.* **1994**, *65* (12), 3793−3798.
(34) Lai, J.; Perazzo, T.; Shi, Z.; Majumdar, A. *Sens. Actuators, A* **1997**, *58* (2), 113−119.
(35) Chu, W. H.; Mehregany, M.; Mullen, R. L. *J. Micromech. Microeng.* **1999**, *3* (1), 4.
(36) Toda, M.; Ono, T.; Liu, F.; Voiculescu, I. *Rev. Sci. Instrum.* **2010**, *81*, 055104.
(37) Tao, H.; Kadlec, E. A.; Strikwerda, A. C.; Fan, K. B.; Padilla, W. J.; Averitt, R. D.; Shaner, E. A.; Zhang, X. *Opt. Express* **2011**, *19* (22), 21620−21626.
(38) Rasool, H. I.; Wilkinson, P. R.; Stieg, A. Z.; Gimzewski, J. K. *Rev. Sci. Instrum.* **2010**, *81*, 2.
(39) Zhu, H.; Yi, F.; Cubukcu, E. *IEEE Photonic Tech. Lett.* **2012**, *24* (14), 1194−1196.
(40) Shchegolkov, D. Y.; Azad, A.; O'Hara, J.; Simakov, E. *Phys. Rev. B* **2010**, *82* (20), 205117.
(41) Wu, C.; Burton Neuner, I.; Shvets, G.; John, J.; Milder, A.; Zollars, B.; Savoy, S. *Phys. Rev. B* **2011**, *84* (7), 075102.
(42) Liu, X. L.; Starr, T.; Starr, A. F.; Padilla, W. J. *Phys. Rev. Lett.* **2010**, *104*, 207403.
(43) COMSOL Multiphysics 4.2a, COMSOL Inc.
(44) Bosman, H.; Lau, Y. Y.; Gilgenbach, R. M. *Appl. Phys. Lett.* **2003**, *82* (9), 1353−1355.
(45) Muhlschlegel, P.; Eisler, H. J.; Martin, O. J. F.; Hecht, B.; Pohl, D. W. *Science* **2005**, *308* (5728), 1607−1609.
(46) Ozisik, M. N. *Heat conduction*, 2nd ed.; J. Wiley: New York, 1993.
(47) Bergman, T. L.; Lavine, A. S.; Incropera, F. P.; DeWitt, D. P. *Fundamentals of heat and mass transfer*; Wiley: New York, 2011.
(48) Roark, R. J. *Formulas for stress and strain*, 5th ed.; Mcgraw-Hill: New York, 1975.
(49) Kruse, P. W. *Uncooled Thermal Imaging: Arrays, Systems, and Applications*; SPIE Press: Bellingham, WA, 2001.
(50) Gabrielson, T. B. *IEEE Trans. Electron Devices* **1993**, *40* (5), 903−909.
(51) Majorana, E.; Ogawa, Y. *Phys. Lett. A* **1997**, *233* (3), 162−168.
(52) *Pyroelectric detector, model LIE-200 with NEP of 3.5nW/Hz$^{1/2}$*, InfraTec GmbH.
(53) Kwon, H.; Kim, S. H.; Yee, Y.; Ha, J. M.; Kim, S. C.; Song, K. C.; Um, K. Y.; Nam, H. J.; Joo, Y. C.; Bu, J. U. *Jpn. J. Appl. Phys. 1* **2007**, *46* (8B), 5473−5477.
(54) Tao, H.; Landy, N. I.; Bingham, C. M.; Zhang, X.; Averitt, R. D.; Padilla, W. J. *Opt. Express* **2008**, *16* (10), 7181−7188.